

# SU(3) Dirac electrons in the 1/5-depleted square-lattice Hubbard model at 1/4 filling

Yasufumi Yamashita,<sup>1,\*</sup> Masaki Tomura,<sup>2</sup> Yuki Yanagi,<sup>2,3</sup> and Kazuo Ueda<sup>2</sup>

<sup>1</sup>College of Engineering, Nihon University, Koriyama, Fukushima 963-8642, Japan

<sup>2</sup>Institute for Solid State Physics, University of Tokyo, Kashiwa, Chiba 277-8581, Japan

<sup>3</sup>Department of Physics, Faculty of Science and Technology,  
Tokyo University of Science, Noda, Chiba 278-8510, Japan

(Received 1 July 2013; revised manuscript received 13 September 2013; published 4 November 2013)

We investigate the magnetic and metal-insulator (M-I) phase diagram of the 1/5-depleted square-lattice Hubbard model at 1/4 filling by the mean-field approximation. There exist three magnetic phases of nonmagnetic (N), antiferromagnetic (AF), and ferromagnetic (F) types, each realized for the large intrasquare hopping  $t_1$ , intersquare hopping  $t_2$ , and Coulomb interaction  $U$ , respectively. Within each magnetic phase, the M-I transition of Lifshitz type emerges and, finally, six kind of phases are identified in the  $U - t_1/t_2$  plane. When  $t_1 = t_2$ , we find that the Dirac cone and nearly flat band around the  $\Gamma$  point form the SU(3) multiplet. The SU(3) effective theory well describes the phase transitions between NI, paramagnetic-metal (PM), and AF phases. The NI and AFI phases are characterized by different Berry phases as in polyacetylene or graphene.

PACS numbers: 71.10.Fd, 71.30.+h, 75.30.Kz, 71.10.-w

## I. INTRODUCTION

In recent years, physics emerging from anomalous dispersion relations, such as a complete flat band or the Dirac cone, have attracted much attention in condensed matter physics.<sup>1-4</sup> For example when the Fermi energy coincides with the flat band, a macroscopic degeneracy in the single electron spectrum allows valence electrons to flip their spins freely without losing extra kinetic energy. In a naive sense, therefore, a ferromagnetism is achieved so as to minimize the Coulomb repulsion energy, unless other instabilities are developed with increasing of the Coulomb interaction. Such a mechanism, so called the flat-band ferromagnetism, is occasionally realized in tight-binding models on geometrically frustrated lattices, generalized line graphs,<sup>5-9</sup> and cell-construction networks.<sup>10,11</sup>

The Dirac cone in material science is frequently discussed for the dispersion around the K and K' points of the honeycomb lattice in graphene,<sup>12,13</sup> where the chiral symmetry prohibits the crossing linear dispersion to be massive.<sup>14,15</sup> Lately, such Dirac electrons are demonstrated to play an important role in the two-dimensional (2D) organic zero-gap semiconductor  $\alpha$ -ET<sub>2</sub>I<sub>3</sub><sup>16,17</sup> or in the surface states of 3D topological insulators.<sup>18,19</sup> Experimentally, the Dirac-cone electronic dispersion is really observed in the Fe-based superconductor BaFe<sub>2</sub>As<sub>2</sub> by ARPES.<sup>20</sup> For the theoretical side, empirically, the Dirac-cone system seems to be commonly found in the nearest-neighbor (NN) tight binding models on regularly depleted lattices. The honeycomb<sup>12</sup> and kagomé<sup>3</sup> lattices are typical examples of such a system, being regarded as the 1/3- and 1/4-depleted triangular lattices, respectively. The half-filled honeycomb-lattice Hubbard model is recently studied intensively in connection with the M-I transition at low temperature.<sup>21,22</sup> The stabilities of charge-ordered states are also investigated for a spinless fermion model on the kagomé lattice at 1/3 filling,<sup>23</sup> which is commensurate due to the lattice depletion. As for square-lattice systems, it is known that the 1/4-depleted square lattice, so called the Lieb model,<sup>5</sup> has flat-band and Dirac-cone dispersions at the same time.

In the present paper, we study the Hubbard model on the 1/5-depleted square lattice, shown in Fig. 1(a), with two different NN hoppings of  $t_1$  and  $t_2$ , representing the intra-

intersquare hoppings, respectively. The original point-group symmetry of this lattice is  $C_4$ , though, as long as the NN hoppings are concerned; one can deform the lattice into the square lattice of diamonds shown in Fig. 1(b). Thus, the point-group symmetry is enlarged into  $C_{4v}$ . In the symmetric case of  $t_1 = t_2 = 1$ , diagonalizing the single-electron part of the Hamiltonian, we find that the lowest  $\alpha$  band and the third  $\gamma$  band form the characteristic Dirac cone at the  $\Gamma$  point [Fig. 1(c)]. The apex of the cone is just located at the 1/4-filling Fermi energy and, moreover, the second band of  $\beta$  intersects this apex at the same time. In this model, therefore, such exotic dispersions emerge simultaneously and, at 1/4 filling, the interplay of them is expected to induce intriguing physics with the inclusion of Coulomb interaction.

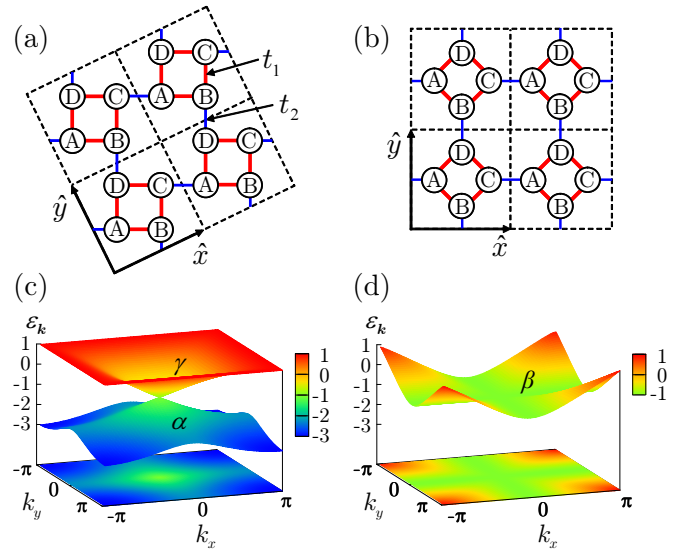


FIG. 1. (Color online) (a) The 1/5-depleted square lattice with the intrasquare ( $t_1$ , thick solid lines) and the intersquare ( $t_2$ , thin solid lines) hoppings. The unit cell, including four distinct sites A, B, C, and D, is enclosed by the dashed-line square connecting four vacant sites. (b) Deformed 1/5-depleted square lattice or decorated square lattice with  $C_{4v}$  symmetry. (c) Dispersion relations  $\epsilon_k$  at  $t_1 = t_2 = 1$  for  $\alpha$  and  $\gamma$  bands, forming the Dirac cone. (d)  $\epsilon_k$  for  $\beta$  band, intersecting the apex of the Dirac cone at the  $\Gamma$  point.

At 1/2 filling with strong electron correlations, this model is reduced to the spin-1/2 Heisenberg model on the 1/5-depleted square lattice which describes the spin-gap phase of  $\text{CaV}_4\text{O}_9$  where the plaquette spin-singlet ground state is realized.<sup>24,25</sup> The ratio of  $J_1/J_2$  ( $\propto t_1^2/t_2^2$ ) controls the spin gap, and quantum phase transitions take place between the plaquette (small  $J_2$ ), classical AF ( $J_1 \sim J_2$ ), and dimer (small  $J_1$ ) phases. Also at 1/4 filling of the present study, electronic states of plaquette or dimer structures give us an intuitive perspective to understand the ground-state phase diagram with respect to  $U$  and  $t_1/t_2$ , as we will see later. It may be worth mentioning that Fe ions in  $\text{K}_{0.8}\text{Fe}_{1.6}\text{Se}_2$  are known to form the 1/5-depleted square lattice, referred to as the  $\sqrt{5} \times \sqrt{5}$  iron-vacancy structure, with  $Q = (\pi, \pi)$  block-AF magnetic ground state.<sup>26</sup>

The paper is organized as follows. In Sec. II we discuss single electron properties focusing on the physics of the SU(3) Dirac cone. In particular, it will become clear that the ways of symmetry lowering from the SU(3) are crucial to give rise to M-I and magnetic transitions as a consequence. After characterizing possible ordered phases in Sec. II, the mean-field phase diagram at low temperature is presented in Sec. III. The NI and AFI phases are further characterized by using the Berry phase in the latter part of this section. Finally we summarize the conclusions and make some remarks in Sec. IV.

## II. SINGLE ELECTRON PROPERTIES

First of all, let us investigate the noninteracting model in search of possible metallic, insulating, and magnetic phases after including external staggered and uniform magnetic fields. Since the Coulomb interaction is mainly treated by the mean-field approximation in the present work, these external fields work as the self-consistent fields reduced from the Hubbard  $U$  term in Sec. III.

### A. Model and dispersion relations

The NN tight-binding model on the 1/5-depleted square lattice is given by  $\mathcal{H}^{(0)} = \sum_{\mathbf{k}\sigma} H_{\mathbf{k}\sigma}^{(0)\alpha\beta} c_{\mathbf{k}\alpha\sigma}^\dagger c_{\mathbf{k}\beta\sigma}$  with

$$\hat{H}_{\mathbf{k}\sigma}^{(0)} = \begin{pmatrix} 0 & t_1 & t_2 e^{-ik_x} & t_1 \\ t_1 & 0 & t_1 & t_2 e^{-ik_y} \\ t_2 e^{+ik_x} & t_1 & 0 & t_1 \\ t_1 & t_2 e^{+ik_y} & t_1 & 0 \end{pmatrix}, \quad (1)$$

where  $c_{\mathbf{k}\alpha\sigma}^\dagger$  creates a spin- $\sigma$  ( $= \pm 1$ ) electron at  $\alpha$  ( $= A - D$ ) sublattice with the momentum  $\mathbf{k} = (k_x, k_y)$ . The eigenvalue equation for Eq. (1) is given by  $F_{\mathbf{k}}(\varepsilon) = 0$  with

$$F_{\mathbf{k}}(\varepsilon) = (\varepsilon^2 - t_2^2)^2 - 4t_1^2 (\varepsilon + t_2 \cos k_x) (\varepsilon + t_2 \cos k_y). \quad (2)$$

The sign reversal of  $t_1$  or  $t_2$  is irrelevant, though the latter shifts the momentum by  $(\pi, \pi)$ , therefore, we assume that  $t_1$  and  $t_2$  are positive definite. For  $t_1 \ll t_2$  and thus  $\varepsilon \simeq \pm t_2$ , at 1/4 filling an electron occupies an antibonding orbital on every  $t_2$  bond, which means the PM ground state. On the other hand, for  $t_1 \gg t_2$  and  $\varepsilon \simeq -2t_1, 0, 0, 2t_1$ , two electrons are confined within a single  $t_1$  square and the  $B_1$  orbital of Eq. (8) is doubly occupied, resulting in the NI ground state. When  $t_1 = t_2$ ,

around the  $\Gamma$  point the functional forms of the Dirac cone ( $\alpha$  and  $\gamma$  bands) and the  $\beta$  band are, respectively, given by

$$\varepsilon_{\mathbf{k}}^{(\alpha/\gamma)} \simeq -t_1 \left( 1 \pm \sqrt{\frac{k_x^2 + k_y^2}{2}} \right), \quad (3)$$

$$\varepsilon_{\mathbf{k}}^{(\beta)} \simeq -t_1 \left\{ 1 - \frac{k_x^2 k_y^2}{2(k_x^2 + k_y^2)} \right\}, \quad (4)$$

as shown in Figs. 1(c) and 1(d). In particular, the bottom of the  $\beta$  band along the  $k_x$  and  $k_y$  axes is completely flat and the system is metallic at 1/4 filling. This is in strong contrast to the standard SU(2) Dirac cone which is a zero-gap semiconductor in a 2D system.

For general  $(t_1, t_2)$ 's, the dispersion relations along  $\Gamma$ -X( $\pi, 0$ )-M( $\pi, \pi$ )- $\Gamma$  are displayed in Fig. 2. As shown in Fig. 2(c), the Dirac cone appears also at the M point, since the relation

$$F_{\mathbf{k}+(\pi, \pi)}(-\varepsilon) = F_{\mathbf{k}}(\varepsilon) \quad (5)$$

holds due to the chiral symmetry. Along the  $\Gamma$ X line, putting  $k_y = 0$  in Eq. (2), a completely flat dispersion emerges at  $\varepsilon = -t_2$ . When the 1/4-filling Fermi energy hits this flat dispersion, for  $t_1 \leq t_2$  as shown in Figs. 2(c)-2(f), the ground state is PM. On the other hand, for  $t_1 > t_2$ , a finite band gap is open at the  $\Gamma$  point as shown in Figs. 2(a) and 2(b). Lifting of the degeneracy at the  $\Gamma$  point seems to be the key to understanding the M-I transition.

### B. SU(3) effective theory

At the  $\Gamma$  point, when  $t_1 = t_2$ , Eq. (1) is diagonalized into  $\text{diag}(3t_1, -t_1, -t_1, -t_1)$  by using the  $C_{4v}$  basis representation of

$$|A_1\rangle = \frac{1}{2}(c_A^\dagger + c_B^\dagger + c_C^\dagger + c_D^\dagger)|0\rangle, \quad (6)$$

$$(|E_x\rangle, |E_y\rangle) = \frac{1}{\sqrt{2}}(c_A^\dagger - c_C^\dagger, c_B^\dagger - c_D^\dagger)|0\rangle, \quad (7)$$

$$|B_1\rangle = \frac{1}{2}(c_A^\dagger - c_B^\dagger + c_C^\dagger - c_D^\dagger)|0\rangle, \quad (8)$$

where  $\mathbf{k}$  and  $\sigma$  indices are abbreviated. The  $|A_1\rangle$  state is energetically separated from the degenerate SU(3) multiplet. Therefore, expanding Eq. (1) for small  $\mathbf{k}$  and  $\mu = t_2/t_1 - 1$ , transforming it into the  $C_{4v}$  basis, and tracing out the  $|A_1\rangle$  state, the effective SU(3) Hamiltonian is constructed for fixed  $\mathbf{k}$  and  $\sigma$  as

$$\mathcal{H}_{\text{eff}}^{(0)} = -\left(1 + \frac{\mu}{3}\right)I_3 - \frac{2\mu}{\sqrt{3}}\lambda_8 + \frac{k_x}{\sqrt{2}}\lambda_5 - \frac{k_y}{\sqrt{2}}\lambda_7 \quad (9)$$

in the unit of  $t_1$ . Here,  $I_3$  and  $\lambda$ 's are, respectively, the identity and the Gell-Mann matrices of the SU(3) subspace spanned by  $(|E_x\rangle, |E_y\rangle, |B_1\rangle)$ .

In the absence of  $\mu$ ,  $\mathcal{H}_{\text{eff}}^{(0)}$  can be viewed as the massless Dirac equation embedded in the SU(3) space. From the  $C_{4v}$  point group symmetry, E and  $B_1$  states are always degenerate to form the Dirac point. Including the mass term proportional to  $\lambda_8 = (|E_x\rangle\langle E_x| + |E_y\rangle\langle E_y| - 2|B_1\rangle\langle B_1|)/\sqrt{3}$ , the accidental degeneracy between E- and  $B_1$ -symmetric states at the  $\Gamma$

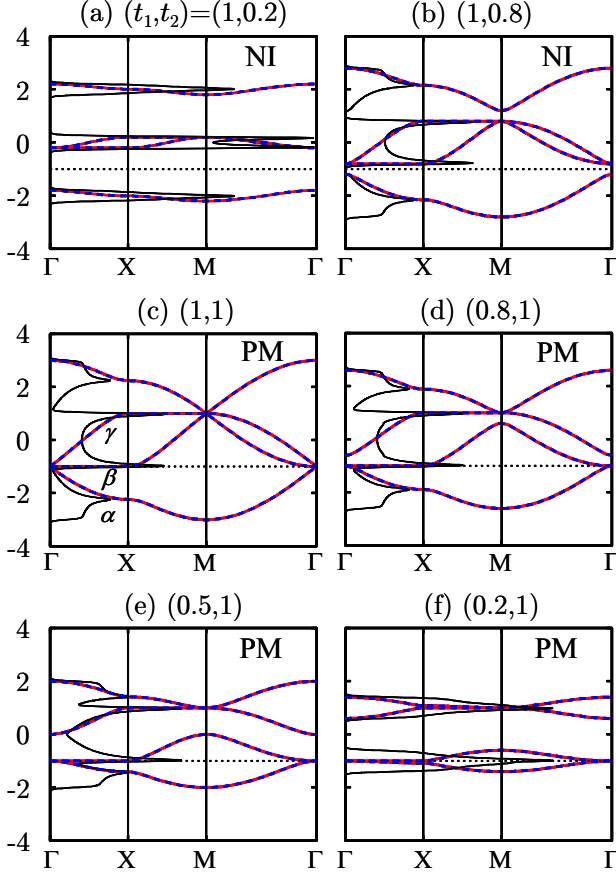


FIG. 2. (Color online) Dispersion relations for spin-up (dashed lines) and spin-down (solid lines) electrons along symmetry lines for various  $(t_1, t_2)$ 's. In the metallic cases of (c), (d), (e), and (f), the flat bands along  $\Gamma$ -X match the Fermi energy, depicted by the dotted line. The densities of states are also displayed.

point is lifted, and a positive (negative)  $\mu$  increases the energy of  $B_1(E)$  state. As a result, Lifshitz transition<sup>27</sup> separates the nonmagnetic phase into NI ( $t_1 > t_2$ ) and PM ( $t_1 \leq t_2$ ) phases, which is consistent with the simple M-I transition picture between the isolated-square ( $t_2 = 0$ , insulating) and isolated-bond ( $t_1 = 0$ , metallic) limits.

### C. Phase diagram under a staggered magnetic field

In order to lift the degeneracy within the E states at the  $\Gamma$  point, we need a  $\lambda_3 = |E_x\rangle\langle E_x| - |E_y\rangle\langle E_y|$  term besides  $\mathcal{H}_{\text{eff}}^{(0)}$ , which can open the charge gap for  $t_2/t_1 \geq 1$  or close it for  $t_2/t_1 < 1$ . For that purpose, we apply the  $\mathbf{Q} = \mathbf{0}$  staggered magnetic field defined by

$$\mathcal{H}^{(B_s)} = \sum_{\mathbf{k}\sigma} \sigma B_s (n_{kA\sigma} - n_{kB\sigma} + n_{kC\sigma} - n_{kD\sigma}), \quad (10)$$

where  $n_{k\alpha\sigma} = c_{k\alpha\sigma}^\dagger c_{k\alpha\sigma}$ . For small  $B_s$ , tracing out the  $|A_1\rangle$  state in the same way, we can easily show that the effective SU(3) model for  $\mathcal{H}^{(B_s)}$ , with fixed  $\mathbf{k}$  and  $\sigma$ , is given by

$$\mathcal{H}_{\text{eff}}^{(B_s)} = \sigma B_s \lambda_3^{(\sigma)}, \quad (11)$$

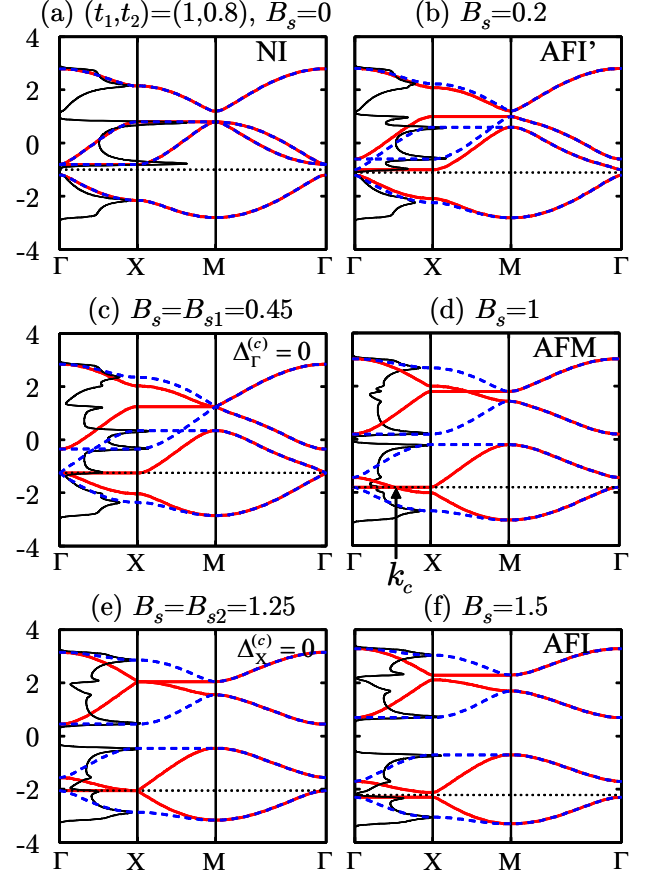


FIG. 3. (Color online) Dispersion relations for  $(t_1, t_2) = (1, 0.8)$  with increasing  $B_s$  from 0 to 1.5, where symbols and lines are the same as in Fig. 2. At  $\mathbf{k} = (k_c, 0)$ , as shown in (d), the flat band is intersected by another band.

where  $\lambda_3^{(\sigma)}$  is the similarly defined Gell-Mann matrix in the spin- $\sigma$  sector. Therefore the  $B_s$  term breaks the E symmetry at the  $\Gamma$  point, which induces M-I phase transitions accompanied by the  $\mathbf{Q} = \mathbf{0}$  AF spin order.

The eigenvalue equation for  $\mathcal{H}^{(0)} + \mathcal{H}^{(B_s)}$  is now written as  $F_{\mathbf{k}}^{(+)}(\epsilon) \cdot F_{\mathbf{k}}^{(-)}(\epsilon) = 0$  with

$$F_{\mathbf{k}}^{(\sigma)}(\epsilon) = \left\{ (\epsilon - \sigma B_s)^2 - t_2^2 \right\} \left\{ (\epsilon + \sigma B_s)^2 - t_2^2 \right\} - 4t_1^2 (\epsilon - \sigma B_s + t_2 \cos k_x) (\epsilon + \sigma B_s + t_2 \cos k_y). \quad (12)$$

Solving Eq. (12), we find the M-I phase diagram<sup>28</sup> in the  $B_s - t_1$  or  $B_s - t_2$  plane as shown in Fig. 4. For  $B_s \neq 0$ , there are two kinds of insulating phases: AFI' (for small  $t_2$ ) and AFI (small  $t_1$ ). In the AFI' phase, like Fig. 3(b), the charge gap  $\Delta_{\mathbf{k}}^{(c)}$  opens at  $\Gamma$ , which is estimated from Eq. (12) to be

$$\Delta_{\Gamma}^{(c)} = -2t_2 - B_s + \sqrt{4t_1^2 + B_s^2}. \quad (13)$$

As shown in Fig. 3(c), the charge gap closes at  $\Delta_{\Gamma}^{(c)} = 0$ , which determines the I-M transition line;

$$B_{s1}(t_1, t_2) = \left( \frac{t_1^2}{t_2} - t_2 \right) \theta(t_1 - t_2). \quad (14)$$

Once entering the metallic phase, like Fig. 3(d), the complete flat band along  $\Gamma$ -X is intersected by the dispersive band at

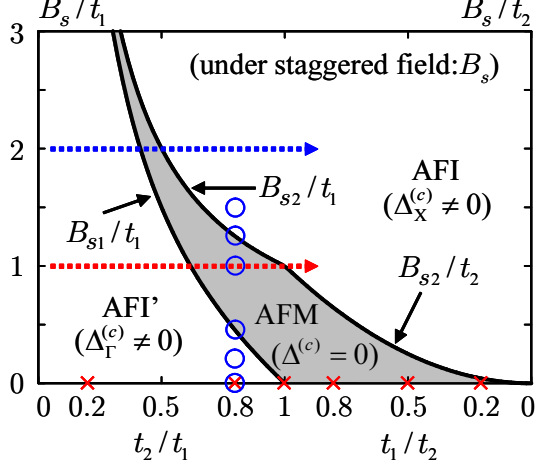


FIG. 4. (Color online) M-I phase diagram<sup>28</sup> under the external staggered magnetic field  $\mathcal{H}^{(B_s)}$ . All transition lines are of Lifshitz type, where only Fermi surface geometry changes and no other symmetry is broken. At the points marked by the crosses ( $\times$ ) and open circles ( $\circ$ ), respectively, the dispersion relations are shown in Figs. 2 and 3. Along the horizontal dashed arrows at  $B_s = t_1$  and  $2t_1$ , the Berry phase is calculated in Fig. 7.

$k_x = k_c$ . The flat band is a localized antibonding orbital of B and D sites with  $\varepsilon = -t_2 - B_s$ , which must be the double root of Eq. (12) at  $\mathbf{k} = (k_c, 0)$  to give,

$$k_c(t_1, t_2, B_s) = 2 \arcsin \sqrt{\frac{B_s}{t_2} \left\{ \frac{t_2^2}{t_1^2} \left( 1 + \frac{B_s}{t_2} \right) - 1 \right\}}. \quad (15)$$

In Fig. 3(d) of  $(t_1, t_2, B_s) = (1, 0.8, 1)$ , for instance,  $k_c$  is calculated to be

$$k_c(1, 0.8, 1) = 2 \arcsin \sqrt{0.55} \simeq 0.53\pi. \quad (16)$$

Note that the dispersive band has even parity with respect to exchanging B and D sites. That's why there is no band splitting at  $\mathbf{k} = (k_c, 0)$ .

With increasing  $B_s$  above  $B_{s1}$ ,  $k_c$  travels from 0 [Fig. 3(c)] to  $\pi$  [Fig. 3(e)], and finally the charge gap of the AFI phase opens at the X point [Fig. 3(f)] with

$$\Delta_X^{(c)} = t_2 + B_s - \sqrt{4t_1^2 + (t_2 - B_s)^2}. \quad (17)$$

Again,  $\Delta_X^{(c)} = 0$  defines the M-I transition line of

$$B_{s2}(t_1, t_2) = \frac{t_1^2}{t_2}, \quad (18)$$

as depicted in Fig. 4. Namely, in the shaded AFM region in Fig. 4,  $k_c$  ranges from 0 to  $\pi$  consistent with the relations,  $k_c(t_1, t_2, B_{s1}) = 0$  and  $k_c(t_1, t_2, B_{s2}) = \pi$ , as shown by using Eqs. (14), (15), and (18).  $B_{s1}$  and  $B_{s2}$  transition lines are of Lifshitz type, which are similar to the PM-NI phase transition at  $B_s = 0$ . Although these M-I transitions are peculiar in that Fermi surfaces of line shape along the  $k_x$  and  $k_y$  axes vanish at the transition.<sup>27</sup>

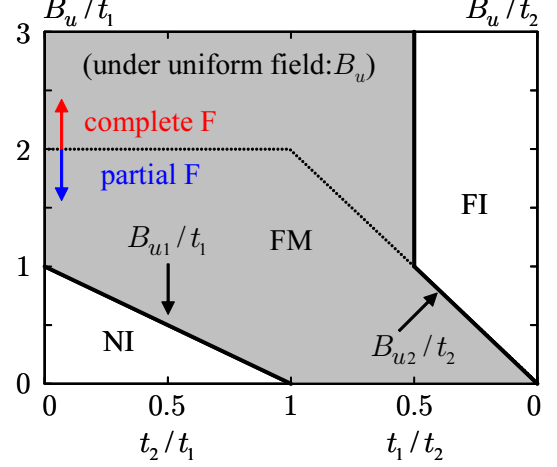


FIG. 5. (Color online) M-I phase diagram<sup>28</sup> under the external uniform magnetic field  $\mathcal{H}^{(B_u)}$ . All transition lines are of Lifshitz type. The dotted line in the FM phase indicates the lower boundary of the complete ferromagnetic region. The ferromagnetic moment in FI is fully saturated.

#### D. Phase diagram under a uniform magnetic field

Figure 5 shows the similarly derived M-I phase diagram<sup>28</sup> under the external uniform magnetic field;

$$\mathcal{H}^{(B_u)} = \sum_{\mathbf{k}\sigma} \sigma B_u (n_{\mathbf{k}A\sigma} + n_{\mathbf{k}B\sigma} + n_{\mathbf{k}C\sigma} + n_{\mathbf{k}D\sigma}). \quad (19)$$

In the NI phase for  $t_2/t_1 < 1$ , the charge gap is given by  $\Delta_\Gamma^{(c)} = 2(t_1 - t_2 - B_u)$ . With increasing  $B_u$  from zero, therefore, the NI-FM phase transition takes place at  $B_{u1} = t_1 - t_2$ . On the other hand, in the FM phase for  $t_1/t_2 \leq 0.5$ , the phase transition to the fully saturated FI phase occurs at  $B_{u2} = 2t_1$ , where  $4t_1$  is the bandwidth of the majority-spin band.

When  $B_u$  is large enough compared with  $t_1$  and  $t_2$ , the present model at  $1/4$  filling is reduced to the spinless  $1/2$ -filled problem. In that case, Fermi energy is zero because of the bipartite symmetry, and the Fermi surface, if it exists, is defined by the equation  $F_{\mathbf{k}}(\varepsilon = 0) = 0$  resulting in

$$\cos k_x \cos k_y = \frac{t_2^2}{4t_1^2}. \quad (20)$$

Therefore,  $t_1/t_2 = 0.5$  determines the FM-FI phase transition line, as shown in Fig. 5 for large  $B_u$ . At this Lifshitz transition, electron and hole pockets at  $\Gamma$  and M points, respectively, vanish simultaneously, see Figs. 2(d)-2(f) at  $1/2$  filling of  $\varepsilon = 0$ .

### III. EFFECTS OF THE COULOMB INTERACTION

#### A. Mean-field phase diagram

Next we consider the effect of the on-site Coulomb interaction within the Hartree-Fock approximation, where the external fields of  $B_s$  and  $B_u$  discussed so far are replaced

by the self-consistent fields. For numerical stabilities, all calculations have been done at a finite temperature of  $T = 0.03 \times \max(t_1, t_2)$  for the typical system size of  $200 \times 200$ . By comparing the free energies of the nonmagnetic, ferromagnetic, and  $\mathbf{Q} = \mathbf{0}$  antiferromagnetic states, we obtain the ground-state phase diagram as shown in Fig. 6. Note that temperature and the system-size dependence of the phase boundaries are already very weak for the present calculations.

We have also checked the paramagnetic susceptibility  $\chi_0(\mathbf{q})$  for  $t_1 < t_2$ , which shows that the leading instability within the random phase approximation (RPA) occurs at  $\mathbf{q} = \mathbf{0}$  and the staggered moments develop within the unit cell consistent with the  $\mathbf{Q} = \mathbf{0}$  AF order assumed in Fig. 4. From the largest eigenvalue of  $\chi_0$ , the RPA instability is determined to be consistent with the PM-AFM transition line shown in Fig. 6. The other simple order parameter, like  $\mathbf{Q} = (\pi, \pi)$  AF order, which is similar to the standard classical AF order in the square lattice, is always high in energy. The other  $\mathbf{Q} = (\pi, \pi)$  mode with the ferromagnetic unit cell, that is the block-AF structure observed in  $\text{K}_{0.8}\text{Fe}_{1.6}\text{Se}_2$ ,<sup>26</sup> has higher energy in this model.

For  $t_1 \simeq t_2$  and small  $U$ , the self-consistent field does not develop and the NI-PM Lifshitz transition at  $t_1 = t_2$  is straight in this region. For  $U \gg t_1$  and  $t_2$ , fully saturated FM and FI compete with each other, separated by the Lifshitz transition at  $t_1/t_2 = 0.5$  consistent with Fig. 5.

On the right half of the phase diagram ( $t_1/t_2 \leq 1$ ) with modest  $U$ , the antiferromagnetic phases prevail over the para- and ferromagnetic phases. Starting from the small  $t_1$  limit, an electron resides on the antibonding orbital of the  $t_2$  bond, labeled by  $i$ , where only the spin degree of freedom  $\mathbf{S}_i$  is left.<sup>29</sup> The second-order perturbation by super-exchange processes via  $t_1$

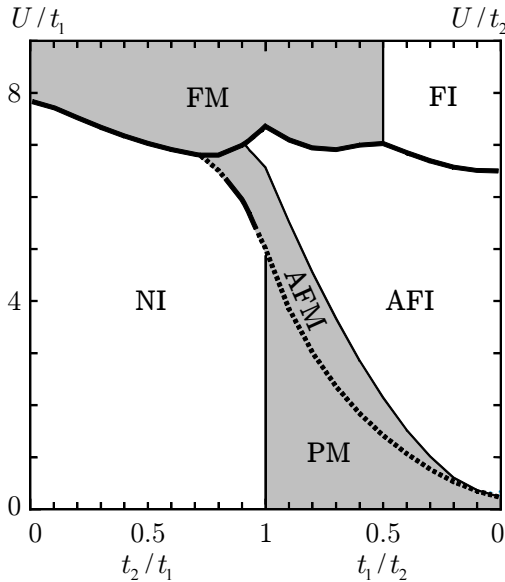


FIG. 6. Mean-field phase diagram in the  $U - t_2$  or  $U - t_1$  plane, where thick-solid and dashed lines represent discontinuous and continuous magnetic phase boundaries, respectively. The symbol AF stands for the  $\mathbf{Q} = \mathbf{0}$  antiferromagnetic order. The ferromagnetic moment in the FM and FI is fully saturated. The M-I phase transition lines shown by thin solid lines are of Lifshitz type.

hoppings derives the effective pairwise spin Hamiltonian,

$$\mathcal{H}_{ij}^{(2)} = \frac{t_1^2}{2} \left( \frac{1}{2t_2 + U} + \frac{4}{U} \right) \mathbf{S}_i \cdot \mathbf{S}_j + \text{const.} \quad (21)$$

Thus, the ground state for the small- $t_1$  region should be the AF bond spin-density wave (SDW) which is consistent with the  $\mathbf{Q} = \mathbf{0}$  AFI of Fig. 6. This is because, in both ordered states, the staggered spin order in the unit cell stretches over the entire lattice uniformly. Once self-consistent fields are developed, there is a one-to-one correspondence between the phase diagrams of Figs. 4, 5, and 6 by reading  $B_s$  or  $B_u$  as  $U$  multiplied by spin densities. Accordingly, the M-I phase boundary in the AF region in Fig. 6 is nothing but the Lifshitz transition discussed in Fig. 4. In addition we have observed a faint trace of the AFI' phase in a narrow region just below the NI-AFM boundary around  $t_2/t_1 = 0.7$ -1.0 (not shown in Fig. 6).

At  $t_2 = 0$ , the model is reduced to the 4-site  $t_1$ -ring+ $U$  problem, in which exact FM and mean-field NI energies of  $E_{\text{FM}}$  and  $E_{\text{NI}}^{(\text{MF})}$ , respectively, are given by

$$E_{\text{FM}} = -2t_1, \quad (22)$$

$$E_{\text{NI}}^{(\text{MF})} = -4t_1 + \frac{U}{4}. \quad (23)$$

Therefore,  $U_c = 8t_1$  is found at  $t_2 = 0$  consistent with the left end of Fig. 6, where the finite  $T$ ,  $0.03t_1$  in the present calculation, decreases the FM free energy and  $U_c$  is slightly reduced. On the other end of Fig. 6 where  $t_1$  is much smaller than  $t_2$  and  $U$ , expanding the FI and AFI mean-field energies as a function of  $t_1$  up to the second order, we obtain

$$E_{\text{FI}}^{(2)} = -2t_2 - \frac{t_1^2}{t_2}, \quad (24)$$

$$E_{\text{AFI}}^{(2)} = -2t_2 - 4t_1^2 \left( \frac{1}{U} + \frac{1}{U + 4t_2} \right). \quad (25)$$

Comparing  $E_{\text{F}}^{(2)}$  and  $E_{\text{AFI}}^{(2)}$ , the mean-field  $U_c$  converges to  $2(1 + \sqrt{5})t_2 \simeq 6.47t_2$  as  $t_1$  approaches zero. The mean-field staggered moment in the AFI is estimated for small  $t_1$  as

$$M_{\text{AFI}}^{(2)} = 1 - 8t_1^2 \left\{ \frac{1}{U^2} + \frac{1}{(U + 4t_2)^2} \right\}. \quad (26)$$

For small  $t_1/t_2$ , in reality, the AFI region extends over  $U = \infty$  because of the super-exchange interaction [Eq. (21)], as mentioned above.

The mean-field analysis is qualitatively justified for the Coulomb interaction  $U$  smaller than the noninteracting bandwidth of  $W = 4t_1 + 2t_2$ . When  $U$  exceeds the maximum bandwidth of around  $6t_1$  or  $6t_2$ , it seems that the first order transitions to fully saturated ferromagnetic states take place mostly irrespective of  $t_1/t_2$ . This may be an artifact due to neglecting electron correlations, though electron kinetic energy is favorable for the spin to be aligned in parallel at  $1/4$  filling, generally speaking.

## B. Calculations of the Berry phase

The AFI' (including the NI as a special case of  $B_s = 0$ ) and AFI phases are also distinguished by using the bulk properties



of Berry phase<sup>30–32</sup> as a function of  $k_x$ , which is defined for  $L_x \times L_y$  lattice under periodic boundary conditions as follows:

$$\gamma_{k_x\sigma}^{(\alpha)} = -i \int_{-\pi}^{\pi} dk_y \langle \Phi_{k\sigma}^{(\alpha)} | \frac{\partial}{\partial k_y} | \Phi_{k\sigma}^{(\alpha)} \rangle \quad (27)$$

$$= \sum_{k_y} \text{Im} \langle \Phi_{k\sigma}^{(\alpha)} | \Phi_{k+(0, \frac{2\pi}{L_y}), \sigma}^{(\alpha)} \rangle, \quad (28)$$

where  $|\Phi_{k\sigma}^{(\alpha)}\rangle$  is the eigenvector of the lowest  $\alpha$  band with spin  $\sigma$ . In the numerical calculations, we take the unit cell as shown in Fig. 1(b) and  $L_x = L_y = 512$ .

Figure 7 displays the numerically evaluated  $\gamma_{k_x,+}^{(\alpha)}$  as a function of  $t_2/t_1$  for fixed values of  $B_s = t_1$  and  $2t_1$ . In the  $B_s - t_2$  plane,  $\gamma_{k_x,+}^{(\alpha)}$ 's are calculated along the dashed arrows as shown in the left-hand side of Fig. 4. With increasing  $t_2/t_1$  for a fixed  $B_s$ , we find that  $\gamma_{k_x,+}^{(\alpha)}$  for  $k_x = 0(\pi)$  jumps from zero to  $\pi$ , like a step function, when  $t_1/t_2$  crosses  $B_s = B_{s1}(B_{s2})$ . Solving  $B_s = B_{s1}$  or  $B_{s2}$  with respect to  $t_2/t_1$  using Eqs. (14) and (18), the critical values of  $t_1/t_2$  for  $k_x = 0$  and  $\pi$  are given by

$$\left(\frac{t_2}{t_1}\right)_{c1} = \sqrt{1 + \left(\frac{B_s}{2t_1}\right)^2} - \frac{B_s}{2t_1}, \quad (29)$$

$$\left(\frac{t_2}{t_1}\right)_{c2} = \left(\frac{B_s}{t_1}\right)^{-1}, \quad (30)$$

respectively. These critical values are indicated by the vertical arrows in Fig. 7 for  $B_s = t_1$  and  $2t_1$ . Eventually, we can reproduce the MI phase diagram shown in Fig. 4 by looking at  $\gamma_{k_x\sigma}^{(\alpha)}$  for  $k_x = 0$  and  $\pi$ .

When  $k_x$  is fixed at an intermediated value between 0 and  $\pi$ , we have numerically found that  $\gamma_{k_x,+}^{(\alpha)} = 0$  for a given parameter set of  $(t_1, t_2, B_s)$ , satisfying  $k_x < k_c(t_1, t_2, B_s)$  and  $\gamma_{k_x,+}^{(\alpha)} = \pi$  otherwise. At  $(t_1, t_2, B_s) = (1, 0.8, 1)$ , for example,  $k_c(t_1, t_2, B_s) \simeq 0.53\pi$ , see Eq. (16) and Fig. 3(d). Therefore,  $\gamma_{0.53\pi,+}^{(\alpha)}$  behaves like  $\pi \cdot \theta(t_2/t_1 - 0.8)$  as a function of  $t_2/t_1$  for  $B_s = t_1$  or like  $\pi \cdot \theta(B_s/t_1 - 1)$  as a function of  $B_s/t_1$  for  $t_2/t_1 = 0.8$ , where  $\theta(x)$  is a step function. In other words, the AFI' (including the NI at  $B_s = 0$ ) and AFI phases are, respectively, characterized by  $\gamma_{k_x\sigma}^{(\alpha)} = 0$  and  $\pi$  for any value of  $k_x$ .

The bulk-edge correspondence<sup>33,34</sup> tells us that the nontrivial Berry phase  $\gamma$  in the AFI suggests an existence of the zero-energy edge state when making a cut on  $t_2$  bonds. Since the wave function in NI(AFI') and AFI phases are mainly confined within the  $t_1$  squares and the  $t_2$  bonds, respectively, then different types of edge state are expected to characterize these two insulating phases. Physics of the edge state lies in the fact that the antibonding orbitals on  $t_2$  bonds are occupied in the AFI phase and, when making a cut, the dangling bonds remain. This is a 2D analog of polyacetylene where the cut on a double covalent bond produces an edge state.<sup>35,36</sup>

#### IV. SUMMARY AND CONCLUDING REMARKS

In summary, we have revealed a rich variety of magnetic and M-I phase diagrams of the 1/5-depleted square-lattice Hubbard model at 1/4 filling within the mean field approximation. The mean-field phase diagram in  $U - t_1$  or  $U - t_2$  plane

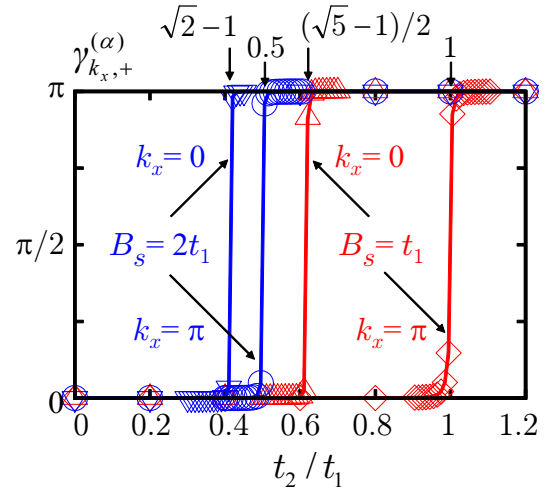


FIG. 7. (Color online) Berry phase  $\gamma_{k_x,+}^{(\alpha)}$  for  $L_x = L_y = 512$  as a function of  $t_2/t_1$  for  $B_s = t_1$  and  $2t_1$  with  $k_x = 0$  and  $\pi$ . We have checked that  $\gamma_{k_x,+}^{(\alpha)}$  converges to a step function as the system size increases. The positions of critical  $(t_2/t_1)_c$  are indicated by vertical arrows.

consists of three magnetic phases of nonmagnetic,  $\mathbf{Q} = \mathbf{0}$  antiferromagnetic, and completely ferromagnetic type. The phase transition between nonmagnetic and antiferromagnetic phases is continuous, which is consistent with the RPA instability for  $t_1 < t_2$ ; the other magnetic transitions to ferromagnetic states are discontinuous. The SU(3) effective theory and the spectrum analyses under the external staggered or uniform magnetic fields elucidate the properties of Lifshitz-type M-I phase transitions in each magnetic phase, which separate the phase diagram into  $3 \times 2 = 6$  parts. In particular, the existence of the AF bond SDW order is shown based on the perturbation theory for small  $t_1$ , which corresponds to an extension of the AFI phase for  $t_1 < t_2$  and  $t_1 \ll U$  in the mean-field phase diagram. When  $U = 0$  and  $t_1 \ll t_2$ , the model is reduced to the 1/2-filled square-lattice tight-binding model of the antibonding orbitals on the  $t_2$  bonds. Then the weak-coupling theory tells us that the perfect nesting leads to the AF SDW insulating order at infinitesimal  $U$ , which corresponds to the very small onset of  $U/t_2$  toward the AFI phase shown in Fig. 6. This AFI phase may be regarded as the two-dimensional analog of the  $4k_F$  charge order discussed in the one-dimensional 1/4-filled Hubbard model for the organic conductor (TMTTF)<sub>2</sub>X.<sup>37,38</sup> In this sense, despite the Hartree-Fock treatment of the present study, we can say that the emergence of the four distinct phases for the small  $U$  region and the hidden symmetry in the AFI phase, which is characterized by the nontrivial Berry phase, should be robust.

One of the most interesting issues to be addressed is whether the FM and FI phases appearing in the large  $U$  region survive or not after including effects of electron correlation beyond the Hartree-Fock approximation. As mentioned for  $t_1 \ll t_2$  and  $U$ , the answer is no. In the opposite limit of  $t_2 = 0, t_1 \ll U$ , unfortunately,  $E_{\text{NI}} = -2\sqrt{2}t_1 < E_{\text{FM}} = -2t_1$  always holds by solving a 4-site Hubbard model with two electrons for no double occupancy. Then what about the case of  $t_1 \simeq t_2 \ll U$ ? To partly answer this question, we have ap-

plied numerical exact diagonalization for the 16-site cluster shown in Fig. 1(a) with eight electrons. For any of open, periodic, and antiperiodic boundary conditions, as a result, the ground-state energy is always found in the spin-singlet sector for  $U$  at least smaller than 20 at  $t_1 = t_2 = 1$ . We need much more sophisticated treatments to settle this issue, which is beyond the scope of this paper.

The Dirac-cone and flat-band dispersions are characteristic of the present model, and the lifting degeneracy of the SU(3) multiplet rules the physics around the SU(3) point. The SU(3) effective Hamiltonian can be constructed solely by the symmetry arguments and, therefore, the present peculiar band structure may be relevant to some realistic cases. For example, complex hopping matrices, like the Haldane model<sup>39</sup> (due to a magnetic flux) or Kane-Mele model<sup>1</sup> (spin-orbit couplings), introduce a  $\lambda_2$  term and a staggered modulation in  $t_1$ 's, due to a lattice symmetry lowering from the original  $C_4$  to  $C_2$ , bringing a  $\lambda_3$  term in the SU(3) model.

The AFM phase is rather specific in that the flat band along  $\Gamma$ -X does not hybridize with the crossing band at  $k_x = k_c$  be-

cause of the different parity symmetry of these two states with respect to exchanging B and D sites.<sup>40</sup> This parity protected AFM phase separates the NI and AFI phases, which are classified according to the different Berry phases. This is the manifestation of the fact that topologically different insulating phases can not be connected unless the charge gap closes at the junction.

## ACKNOWLEDGMENTS

The authors would like to thank H. Tsunetsugu, M. Oshikawa, I. Maruyama, and K. Ohgushi for valuable comments and discussions. This work has been supported by a Grant-in-Aid for Scientific Research on Innovative Areas "Heavy Electrons" (Grant No. 20102008) and (C) (Grant No. 25400357) from the Ministry of Education, Culture, Sports, Science and Technology, Japan. This work was carried out by the joint research in the Institute for Solid State Physics, the University of Tokyo.

\* yamasita@ge.ce.nihon-u.ac.jp

<sup>1</sup> C.L. Kane, and E.J. Mele: Phys. Rev. Lett. **95**, 146802 (2005).

<sup>2</sup> D. Pesin, and L. Balents: Nat. Phys. **6**, 376 (2010).

<sup>3</sup> H.-M. Guo, and M. Franz: Phys. Rev. B **80**, 113102 (2009).

<sup>4</sup> A. Zhao, and S.Q. Shen: Phys. Rev. B **85**, 085209 (2012).

<sup>5</sup> E.H. Lieb: Phys. Rev. Lett. **62**, 1201 (1989).

<sup>6</sup> A. Mielke: J. Phys. A: Math. Gen. **24**, L73, 3311 (1991).

<sup>7</sup> K. Kusakabe and H. Aoki: Physica B **194-196**, 215 (1994).

<sup>8</sup> Y. Yanagi, Y. Yamashita and K. Ueda: J. Phys. Soc. Jpn. **81**, 123701 (2012).

<sup>9</sup> S. Miyahara, K. Kubo, H. Ono, Y. Shimomura, and N. Furukawa: J. Phys. Soc. Jpn. **74**, 1918 (2005).

<sup>10</sup> H. Tasaki: Phys. Rev. Lett. **69**, 1608 (1992).

<sup>11</sup> A. Mielke, and H. Tasaki: Commun. Math. Phys. **158**, 341 (1993).

<sup>12</sup> A.H. Castro Neto, F. Guinea, N.M.R. Peres, K.S. Novoselov and A.K. Geim: Rev. Mod. Phys. **81**, 109 (2009).

<sup>13</sup> M. Fujita, K. Wakabayashi, K. Nakada, and K. Kusakabe: J. Phys. Soc. Jpn. **65**, 1920 (1996).

<sup>14</sup> J.C. Slonczewski, and P.R. Weiss: Phys. Rev. **109**, 272 (1958).

<sup>15</sup> Y. Hatsugai: J. Phys.: Conf. Ser. **334**, 012004 (2011).

<sup>16</sup> S. Katayama, A. Kobayashi, Y. Suzumura, J. Phys. Soc. Jpn. **75**, 054705 (2006).

<sup>17</sup> N. Tajima, S. Sugawara, R. Kato, Y. Nishio, and K. Kajita, Phys. Rev. Lett. **102**, 176403 (2009).

<sup>18</sup> M.Z. Hasan, and C.L. Kane, Rev. Mod. Phys. **82**, 3045 (2010).

<sup>19</sup> J.E. Moore, Nature (London) **464**, 194 (2010).

<sup>20</sup> P. Richard, K. Nakayama, T. Sato, M. Neupane, Y.-M. Xu, J. H. Bowen, G. F. Chen, J. L. Luo, N. L. Wang, X. Dai, Z. Fang, H. Ding, and T. Takahashi: Phys. Rev. Lett. **104**, 137001 (2010).

<sup>21</sup> Z.Y. Meng, T.C. Lang, S. Wessel, F.F. Assaad, and A. Muramatsu, Nature (London) **464**, 847 (2010).

<sup>22</sup> S. Sorella, Y. Otsuka, and S. Yunoki, Scientific Reports **2**, 992

(2012).

<sup>23</sup> S. Nishimoto, M. Nakamura, A. O'Brien, and P. Fulde, Phys. Rev. Lett. **104**, 196401 (2010).

<sup>24</sup> K. Ueda, H. Kontani, M. Sigrist, and P.A. Lee: Phys. Rev. Lett. **76**, 1932 (1996).

<sup>25</sup> M. Troyer, H. Kontani, and K. Ueda: Phys. Rev. Lett. **76**, 3822 (1996).

<sup>26</sup> W. Bao, Q. Huang, G.F. Chen, M.A. Green, D.M. Wang, J.B. He, X.Q. Wang, and Y. Qiu: Chin. Phys. Lett. **28**, 086104 (2011).

<sup>27</sup> I.M. Lifshitz: Sov. Phys. JETP **11**, 1130 (1960) [Zh. Eksp. Teor. Fiz. **38**, 1569 (1960)].

<sup>28</sup> Here, AF (F) stands for the staggered (uniform) spin polarization under the  $B_s$  ( $B_{||}$ ) field. We use this terminology for the external field induced phase to be consistent with the mean-field phase diagram shown in Fig. 6.

<sup>29</sup> Since  $t_2$  is positive definite, the antibonding orbital is located lower in energy.

<sup>30</sup> M.V. Berry, Proc. R. Soc. London, Ser. A **392**, 45 (1984).

<sup>31</sup> J. Zak, Phys. Rev. Lett. **62**, 2747 (1989).

<sup>32</sup> R. Resta, Rev. Mod. Phys. **66**, 899 (1994).

<sup>33</sup> B.I. Halperin, Phys. Rev. B **25**, 2185 (1982).

<sup>34</sup> Y. Hatsugai, Solid State Comm. **149**, 1061 (2009).

<sup>35</sup> W.P. Su, J.R. Schrieffer, and A.J. Heeger: Phys. Rev. Lett. **42**, 1698 (1979).

<sup>36</sup> S. Ryu, and Y. Hatsugai, Phys. Rev. Lett. **89**, 077002 (2002).

<sup>37</sup> D. Jérôme, Chem. Rev. **104**, 5565 (2004).

<sup>38</sup> K.C. Ung, S. Mazumdar, and D. Toussaint, Phys. Rev. Lett. **73**, 2603 (1994).

<sup>39</sup> F.D.M. Haldane, Phys. Rev. Lett. **61**, 2015 (1988).

<sup>40</sup> H. Tsunetsugu: private communication.